Naval Research Laboratory
Washington, DC 20375-5320

NRL/6880/MR—2023/1

Integration of 2D Semiconductors and Hexagonal Boron Nitride as a Platform For Future Quantum Photonics

SAMUEL W. LAGASSE

Power and Advanced Materials Branch
Electronics Science and Technology Division

June 12, 2023

REPORT DOCUMENTATION PAGE

Form Approved
OMB No. 0704-0188

1. REPORT DATE *(DD-MM-YYYY)* 12-06-2023	**2. REPORT TYPE** NRL Memorandum Report	**3. DATES COVERED** *(From - To)* 11/8/2021 – 11/7/2022

4. TITLE AND SUBTITLE

Integration of 2D Semiconductors and Hexagonal Boron Nitride as a Platform For Future Quantum Photonics

5a. CONTRACT NUMBER

5b. GRANT NUMBER

5c. PROGRAM ELEMENT NUMBER
NISE

6. AUTHOR(S)

Samuel W. LaGasse

5d. PROJECT NUMBER

5e. TASK NUMBER

5f. WORK UNIT NUMBER
N20W

7. PERFORMING ORGANIZATION NAME(S) AND ADDRESS(ES)

Naval Research Laboratory
4555 Overlook Avenue, SW
Washington, DC 20375-5320

8. PERFORMING ORGANIZATION REPORT NUMBER

NRL/6880/MR--2023/1

9. SPONSORING / MONITORING AGENCY NAME(S) AND ADDRESS(ES)

Naval Research Laboratory
4555 Overlook Avenue, SW
Washington, DC 20375-5320

10. SPONSOR / MONITOR'S ACRONYM(S)

NRL-NISE

11. SPONSOR / MONITOR'S REPORT NUMBER(S)

12. DISTRIBUTION / AVAILABILITY STATEMENT

DISTRIBUTION STATEMENT A: Approved for public release; distribution is unlimited.

13. SUPPLEMENTARY NOTES

Karles Fellowship

14. ABSTRACT

This report presents research conducted by Samuel W. LaGasse as part of a Jerome and Isabelle Karle Distinguished Scholar Fellowship between November 2021 and 2022. This work investigates the optical properties of layered 2D materials with a focus on gaining control over them in two ways (1) by electrostatic gating and (2) by a novel waveguiding approach. The major output of this fellowship is fundamental knowledge of factors governing atomically thin semiconductors (transition metal dichalcogenides, or TMDs) embedded in slabs of insulating hexagonal boron nitride (hBN). Monolayer TMDs host excitons that behave as either in-plane and out-of-plane optical dipoles. The intricate coupling of such dipoles to slab waveguide modes of hBN is elucidated. The usage of such slab waveguides is further characterized with Fourier spectroscopy, highlighting how this approach can be used to study dipoles in layered materials. Electrostatic gating is used to tune the ratios of in-plane and out-of-plane dipoles, as well as the specific excitonic charge states which are observed. The slab waveguide approach leads to extremely high-quality optical samples, which have future applications as sensors or in quantum information. This work is the topic of a manuscript which is to be submitted in FY23.

15. SUBJECT TERMS

2D materials	Waveguide
Transition metal dichalcogenides	Nanoscience

16. SECURITY CLASSIFICATION OF:			**17. LIMITATION OF ABSTRACT**	**18. NUMBER OF PAGES**	**19a. NAME OF RESPONSIBLE PERSON** Samuel W. LaGasse
a. REPORT U	**b. ABSTRACT** U	**c. THIS PAGE** U	U	23	**19b. TELEPHONE NUMBER** *(include area code)* (202) 404-4574

CONTENTS

This page intentionally left blank.

EXECUTIVE SUMMARY

This report presents research conducted by Samuel W. LaGasse as part of a Jerome and Isabelle Karle Distinguished Scholar Fellowship between November 2021 and 2022. This work investigates the optical properties of layered 2D materials with a focus on gaining control over them in two ways (1) by electrostatic gating and (2) by a novel waveguiding approach. The major output of this fellowship is fundamental knowledge of factors governing atomically thin semiconductors (transition metal dichalcogenides, or TMDs) embedded in slabs of insulating hexagonal boron nitride (hBN). Monolayer TMDs host excitons that behave as either in-plane and out-of-plane optical dipoles. The intricate coupling of such dipoles to slab waveguide modes of hBN is elucidated. The usage of such slab waveguides is further characterized with Fourier spectroscopy, highlighting how this approach can be used to study dipoles in layered materials. Electrostatic gating is used to tune the ratios of in-plane and out-of-plane dipoles, as well as the specific excitonic charge states which are observed. The slab waveguide approach leads to extremely high-quality optical samples, which have future applications as sensors or in quantum information. This work is the topic of a manuscript which is to be submitted in FY23.

This page intentionally left blank.

INTEGRATION OF 2D SEMICONDUCTORS AND HEXAGONAL BORON NITRIDE AS A PLATFORM FOR FUTURE QUANTUM PHOTONICS

1. INTRODUCTION

The layered insulator hexagonal boron nitride (hBN) is a critical substrate that brings out the exceptional intrinsic properties of two-dimensional (2D) materials such as graphene and transition metal dichalcogenides (TMDs). In this work, we demonstrate how hBN slabs tuned to the correct thickness will act as optical waveguides, which enables direct optical coupling of light emission from encapsulated layers into waveguide modes. We integrate two types of TMD monolayers ($MoSe_2$ and WSe_2) within hBN-based waveguides and demonstrate direct coupling of photoluminescence emitted by in-plane and out-of-plane dipoles (bright and dark excitons) to slab waveguide modes. Fourier plane imaging of waveguided photoluminescence from $MoSe_2$ demonstrate that dry etched hBN edges are an

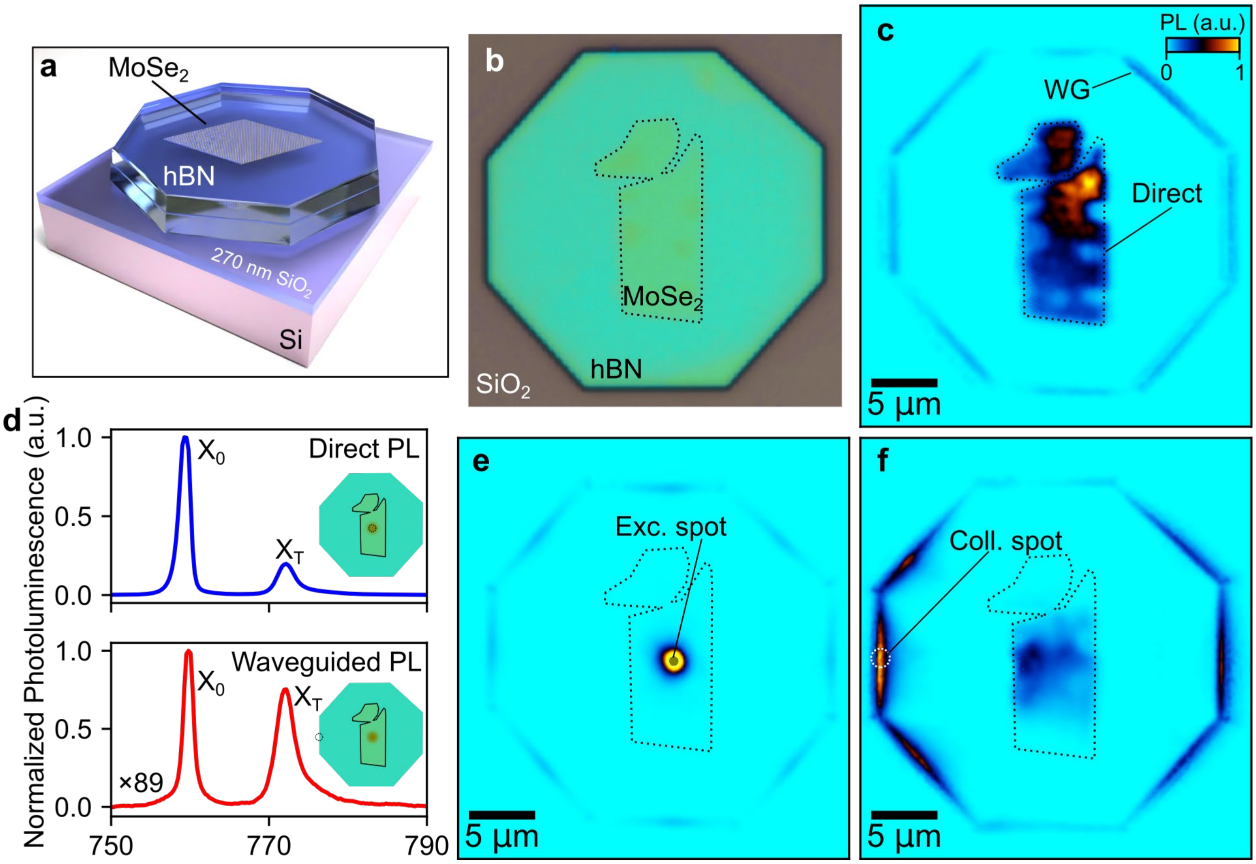

Figure 1: Waveguiding of MoSe2 PL in a hBN slab waveguide. (a) 3D schematic of Sample #1, consisting 85 nm top hBN/monolayer $MoSe_2$/164 nm bottom hBN/270 nm thermal SiO_2/Si wafer. The sample is etched into an octagonal shape. (b) Optical image of Sample #1. (c) Scanning PL measurement of Sample #1; typical PL is observed when scanning over the monolayer $MoSe_2$ flake. PL is also observed when the laser is scanned over the BN edge, which is a result of the excitation laser coupling into the hBN waveguide, exciting the sample, and then emitted PL waveguiding back out and outcoupling to the objective. (d) Low temperature PL spectra of $MoSe_2$ in both direct (top) and waveguiding channels (bottom). The laser and collection spots are shown as insets. (e) Confocal PL map with a fixed excitation spot held on the $MoSe_2$ (labeled) and a scanned collection spot. (f) Confocal PL map with a fixed collection spot (labeled) and a scanned excitation spot.

Manuscript approved June 1, 2023.

effective out-coupler of waveguided light without the need for oil-immersion optics. Gated photoluminescence of WSe_2 demonstrates the ability of hBN waveguides to collect light emitted by out-of-plane dark excitons and trions. In-depth optical simulations explore the parameters of dipole placement and total slab thickness, elucidating the critical design parameters and serving as a guide for novel devices implementing hBN slab waveguides that broaden the 2D material toolkit. Our results provide a simple route for waveguide-based interrogation of layered materials, as well as a way to integrate layered materials into future photonic devices at arbitrary positions whilst maintaining their intrinsic properties.

The optical properties of two-dimensional (2D) materials and their heterostructures are of fundamental importance due to their reduced dimensionality and thus have received a great deal of attention.[1,2] 2D materials are predicted to have a wide range of applications in optoelectronics,[3] photonics,[4,5] nonlinear optics, and quantum information.[6] Therefore, the ability to optically address layered materials on-chip without compromising their properties is key to utilizing them in these applications. It is well established that the surface-like nature of 2D materials makes them particularly susceptible to extrinsic effects such topographic and electronic disorder,[7–11] as well as environmental degradation.[12–14] Hexagonal boron nitride (hBN), a layered insulator with an ultra-flat surface, has emerged as the ideal substrate for 2D materials.[15–17] Encapsulation with hBN provides a protective dielectric environment[18–20] for embedded 2D layers and enables measurement of their intrinsic properties.[9,21–25]. Layers of hBN adhere strongly to other 2D materials, a crucial feature enabling the van der Waals assembly processes.[24] Indeed, the use of hBN encapsulation to provide a low-disorder environment for 2D materials has become ubiquitous.[9] Careful manipulation of hBN has also been used for selective tearing and stacking of twisted homobilayers,[26] which has driven the twistronics revolution, including the discovery of magic-angle graphene.[27,28] Recently, strongly correlated physics has experienced a 2D moiré material renaissance,[29–35] where most studies includes hBN layers for passivation, gate dielectrics, and even tunnel barriers and spacers. Other materials have also benefitted from passivation with hBN capping layers, such as carbon nanotubes[36,37] and layered perovskite crystals.[38–40] Additionally, hBN has proven interesting in its own right, housing visible single photon emitters,[41–44] spin-polarized defects,[45] and behaving as a hyperbolic material and waveguide in the mid-infrared.[46,47] In this work we demonstrate another feature of hBN, wherein layers of hBN used in 2D heterostructure stacking serve another role as a built-in slab waveguide for enhancing optical spectroscopy of and giving control over optical interactions of encapsulated 2D semiconductors.

Transition metal dichalcogenides are layered semiconductors with strong exciton binding energies, low dielectric screening, and large optical constants.[48–52] The conduction band splitting of monolayer WX_2 TMDs (X = Se or S) results in the recombination of the lowest energy state of the K-valley being spin-disallowed, giving rise to a ground state dark exciton which spans the K to K^- valley[53]. These dark excitons recombine radiatively through an out-of-plane (OP) dipole transition, which results in in-plane light emission with a toroidal pattern that makes their PL emission difficult to measure in a standard microscope configuration. There have been successful strategies for coupling dark exciton emission into external structures which can then outcouple light to a detector, including using plasmonic enhancement,[54,55] single-crystal silver plasmonic waveguides,[56] localized strain,[57] or GaSe slab waveguides,[58] however, each of these techniques has an experimental cost associated with their execution. In each case, monolayer semiconductors are either used directly or layered with hBN and other 2D materials such as few-layer graphite (FLG) and then laminated onto or draped over the coupling element. These processes can have unintentional side effects on the 2D semiconductor and often induce charge doping, strain, and add significant fabrication complexity. Recently, hBN-based waveguides and resonators integrated with TMDs have received some attention[59,60], which presents a pathway towards guiding light emitted by dark excitons that we explore here. Additionally, evidence has been reported that interlayer excitons in stacked layers of TMDs also emit via an OP dipole transition,[61] and similar results have been shown for multi-layers of InSe[62]. Therefore, a method to laterally couple light into and out of layered materials will be of great use for both fully understanding their optical properties and harnessing them for applications.

In this work, we present a simple solution to this problem by utilizing hBN slabs as optical waveguides (WGs). By embedding optical emitters (such as monolayer semiconductors) within hBN slabs, we can directly couple emitted light into the fundamental WG modes, rather than through near-field evanescent coupling. We present pilot studies on monolayer $MoSe_2$ (Sample #1) and WSe_2 (Sample #2), and we find that both photoluminescence (PL) and Raman can be detected via optical guiding in hBN. Excitons with in-plane (IP) dipole orientation, such as the bright excitons in $MoSe_2$, couple into transverse electric (TE) WG modes. Conversely, the dark exciton and trion of WSe_2, which behave as OP dipoles, couple to transverse magnetic (TM) WG modes. We use angle-resolved PL measurements to show how Fourier plane filtering of guided light can further discriminate emission from different IP and OP states. Our results are confirmed by comprehensive optical simulations that elucidate the dipole emitter orientation- and position-dependent coupling into different WG modes. These simulations provide simple "rule of thumb" conditions for designing future studies utilizing optical guiding in hBN slabs. We envision the ease of use of hBN slab waveguides in augmenting 2D materials spectroscopy will lead to their rapid adoption in advanced studies of layered materials, as well as their integration with nanophotonic devices.

2. EXPERIMENTAL RESULTS

Coupling light between a free-space and a wave-guided mode is typically achieved at the edge of a material, where the specific boundary conditions for the propagating light wave can be satisfied.[63] Knowing this, we designed an hBN stack with multiple edge facets to test different WG geometries (Fig 1a). As our embedded light source we choose $MoSe_2$, which has a bright exciton (IP dipole) as its lowest energy transition. We construct a simple hBN/$MoSe_2$/hBN stack (Fig. 1A) that is laminated onto a 270 nm thermal SiO_2/Si substrate. The stack is etched into an octagonal shape, where each of the facets can be used to both inject excitation laser light and collect emitted PL from the encapsulated $MoSe_2$ monolayer, and can inform on polarization properties without the need to rotate the sample.

On this structure, we perform conventional micro-PL mapping (Fig. 1c), which shows not only the standard PL at the $MoSe_2$ flake, but also a strong signal whenever the laser is scanned over the hBN edge away from the $MoSe_2$ flake. This 'edge signal' is the result of the excitation laser coupling into the hBN slab, waveguiding to the $MoSe_2$ and exciting PL, and then PL coupling back through the hBN slab and out to the spectrometer. The spectral features from both the direct and edge-coupled PL are typical of $MoSe_2$ at 4.5K, including the neutral (X_0) and charged exciton (X_T) with sharp linewidths around 3 meV (Fig. 1d). The existence of sharp linewidths from the waveguide-based collection channel indicates that it is possible to integrate TMDs with hBN slab waveguides without disturbing their intrinsic properties. To further visualize the waveguiding phenomenon, we then modified the PL setup by decoupling the excitation and collection spots using dual scanning mirrors. In one experiment, we fix the excitation spot in the center of the sample and scan the collection spot, showing the spatial extent of both local and edge-collected PL (Fig. 1e). In another experiment, we fix the collection spot on the hBN edge and scan the excitation spot, showing the extent and directionality of the edge-collected PL (Fig. 1f). Our confocal PL measurements demonstrate how hBN slab WGs provide an effective means of probing encapsulated monolayers through direct and edge-coupled excitation and collection without compromising the intrinsic properties of the optical emitter.

The polarization and directionality of waveguided light out-coupled at hBN edges informs on the usefulness of hBN WGs for possible optoelectronic device applications. To gain further insights into the operation of our slab WG approach, we perform room temperature polarization-resolved widefield PL imaging. The entire $MoSe_2$ flake is illuminated with a broad 514 nm laser spot and emitted PL is imaged by a charge-coupled device (CCD) array (Fig. 2a). Additionally, we analyze the collected PL with a linear polarizer set vertical (Fig. 2b) or horizontal (Fig. 2c) with respect to the sample. We observe strong PL from the edges of the hBN slab which are parallel to the axis of the polarizer, whilst partial extinction of the PL is observed for the edges which are at 45°, and nearly full extinction when the edges are perpendicular to the polarizer. These results show light which is out-coupled by the hBN slab edge has a linear polarization which is parallel to the out-coupling edge.

It is valuable to understand the mechanism of how the simple hBN edge in of our WG structure behaves as an out-coupler for guided light. Fourier plane imaging is a technique that measures the far-field propagation angle of light emitted by a sample. The angle of propagating light, θ, measured relative to our sample plane is related to the wavevector k on the Fourier plane by $k/k_0 = n \sin\theta$ (with $n = 1$ in our measurements and k_0 the in-plane wavevector in air). We apply Fourier plane imaging here to show how effective the hBN edge is at re-directing in-plane propagating PL out and up to the far field, depicted schematically in Fig. 2d. Fig. 2e shows the corresponding Fourier plane measurement for the unpolarized widefield image in Fig. 2a, providing a baseline view of the angle of PL emission, with the maximum values of k restricted to 0.8 by the numerical aperture (NA) of our objective. Here, we measure a strong and symmetrical signal emitted primarily normal to the sample plane ($k = 0$). We selectively image PL emitted at the hBN slab edges by introducing a spatial filtering aperture at a real-space image plane (Fig. 2f and g). We make use of the polarization control provided by the edges of our octagonal hBN slab to sample the parallel and perpendicular polarization states of the edge emission simply by using a horizontal linear polarizer and collecting from the top (Fig. 2f) or right edge (Fig. 2g) of the sample, respectively. The strongest PL is observed in the parallel configuration (Fig. 2f), in agreement with the widefield imaging. In contrast to the overall Fourier plane measurement

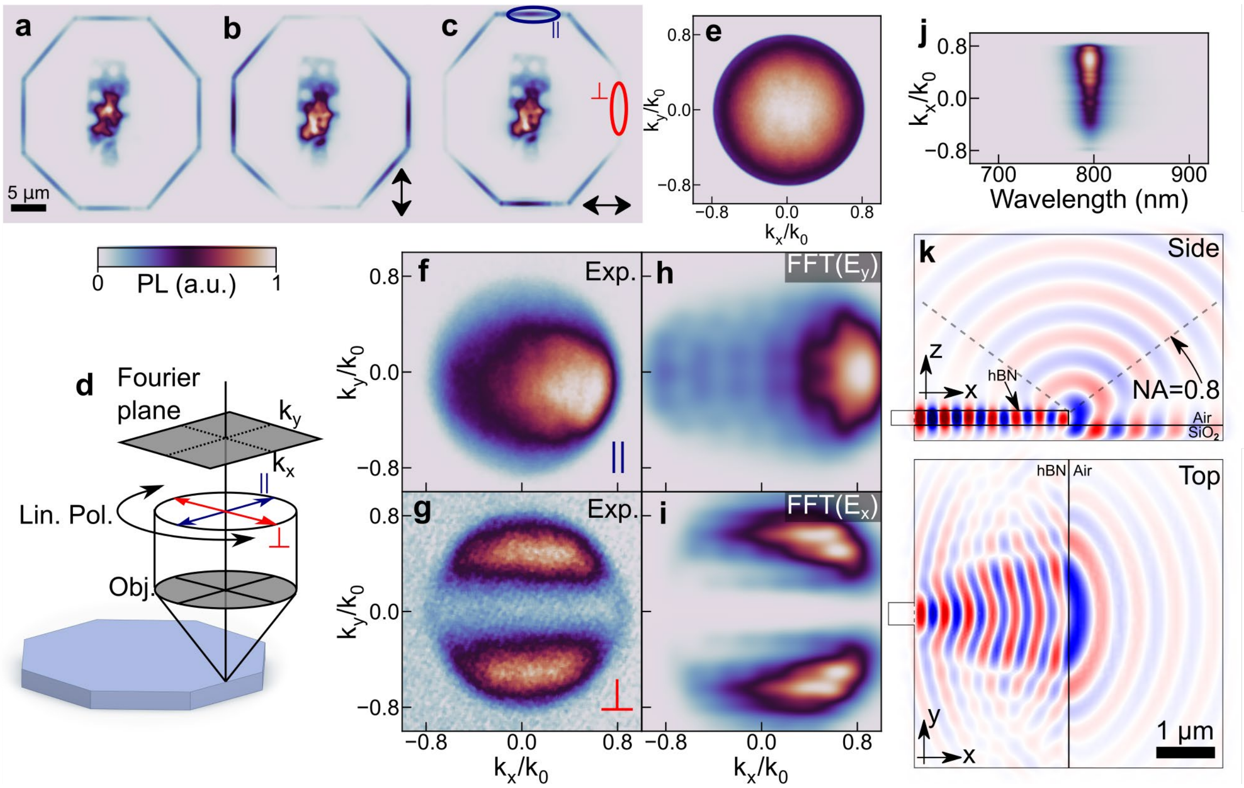

Figure 2: Polarization-resolved and Fourier plane imaging. Widefield PL imaging performed with (a) no polarization filter, (b) a vertical polarization, and (c) a horizontal polarization. (d) Schematic of Fourier plane measurement for waveguide-coupled PL. A linear polarizer is fixed either perpendicular (red arrow) or parallel (blue arrow) to the hBN edge. (e) Fourier plane image of widefield PL shown in (a). Fourier plane images of waveguided PL are captured in the parallel (f) and perpendicular (g) configurations by measuring on the facets labeled in (c). The image in (f) is rotated 90° such that both measurements follow the schematic in (e) with the k_X axis oriented perpendicular to the edge. (h,i) 2D FFTs of a 3D electromagnetic simulations of edge-emitted light at 770 nm. (j) Unpolarized spectrally-resolved Fourier image of waveguided PL emitting from the hBN slab edge. The k-axis is oriented perpendicular to the sample edge. (k) Side views of simulated electric field E_y for a TE_0 guided mode injected by a port (depicted as a small box extending to the left). A dashed line in the top panel indicates the acceptance cone of the 0.8 NA objective used in our experimental setup.

in Fig. 2e, the edge-coupled PL emits with an angular pattern that results from the trajectory of the waveguided light being bent up towards our objective. With the polarizer perpendicular to the hBN edge (Fig. 2g) we observe a weaker signal with two lobe-like patterns which peak coaxially with the hBN edge. This weaker signal, which would typically not be observed for a pure TE guided mode in a narrow monolithic waveguide, deserves special attention and relates to the fact that our sample permits many slab modes which propagate with various angles.

To support our understanding of the nature of waveguided light out-coupled from hBN edges, we use classical electromagnetic modeling implemented in COMSOL (see computational methods, SI Section S1). For the IP dipole of $MoSe_2$, we simulate a TE_0 guided mode at 770 nm in a semi-infinite waveguide and couple it to a large simulation volume visualize its propagation (Fig. 2k). When the guided light enters the larger cell, it spreads in a cone-like shape, resulting in light propagating with a broad range of angles arriving at the hBN edge. The light scatters out to the far-field upon reaching the edge of the hBN slab. To extract the simulated angular emission pattern from the hBN edge, we perform a 2D FFT on the simulated electric field in a plane just above the hBN surface (Fig. 2h, i). The simulated Fourier images capture the essential components of the experimental results, with some additional interference patterns due to the phase coherence of the simulation.

Our simulations indicate that both configurations observed in the polarization-resolved Fourier images stem from light guided in a TE mode. For light polarized parallel to the edge, the strong edge-coupled PL is contributed from IP dipoles that are oriented parallel to the hBN edge. Conversely the weaker PL observed when the polarizer is perpendicular to the edge is due to emission from IP dipoles, which are oriented at oblique angles to the hBN edge. Emission from these off-angle dipoles arrives at the hBN edge with momentum *k*-vector components that allow for out-coupling into the crossed polarizer channel, which one might normally assume is reserved for only TM guided light. While we expect a uniform distribution of dipole emitter in-plane angles within our measurements, the outcoupling efficiency is reduced for light propagating off-normal to the hBN edge, which gives rise to the weaker signal observed in the crossed-polarization configuration.

We have seen how hBN WGs can be used to study in-plane dipoles in $MoSe_2$; we now shift our focus to monolayer WSe_2, which hosts an OP dipole, the dark exciton, in its ground state energy transition. The lateral (in-plane) PL emission of OP dipoles makes them a good candidate for testing differences in dipole orientation and coupling efficiency to hBN slab waveguides. Since WSe_2 excitons are very sensitive to their environmental charge state, and the dark exciton only exists near charge neutrality, we include a few-layer graphene (FLG) back gate in Sample #2 that allows for continuous tuning of the carrier density (Fig. 3a). We also constructed Sample #2 on a glass substrate to show versatility in the overall structure design. Using the same PL scanning geometry as in Figure 1e (i.e., fixed excitation spot and scanning collection spot), Fig. 3b shows a confocal PL image of WSe_2 taken at 4.5 K. From this map, we measure strong PL intensity when the collection spot overlaps with the excitation spot (i.e., local PL), as

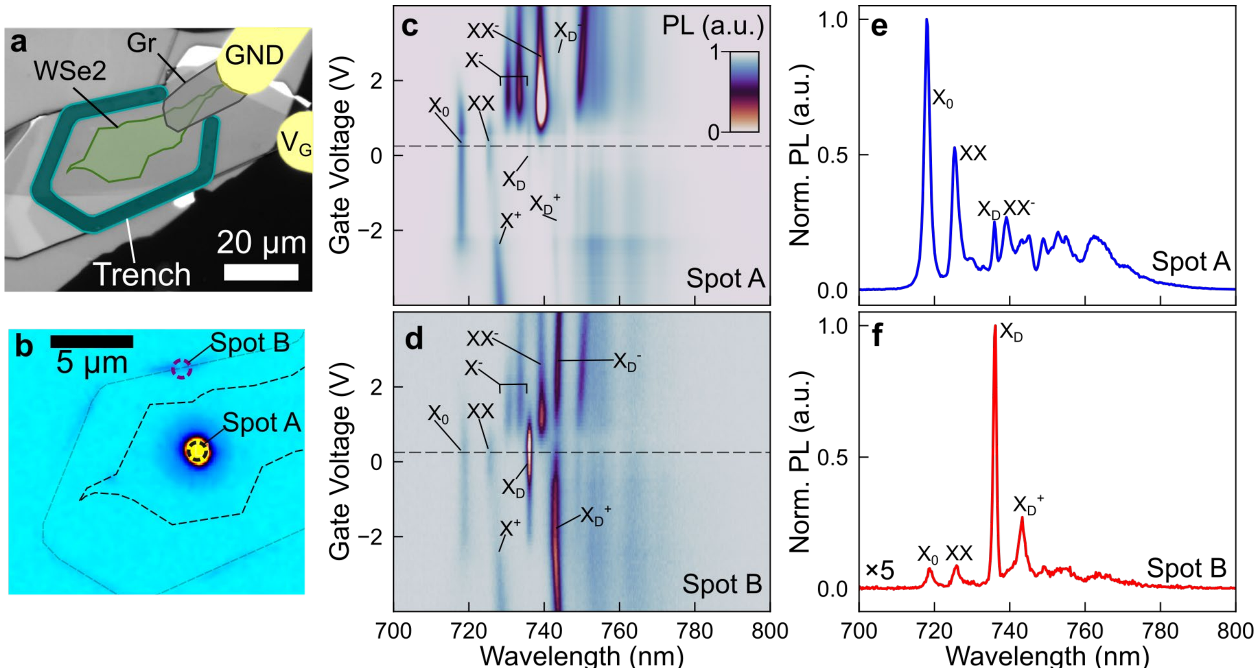

Figure 3: Waveguiding of OP dipoles; dark excitons in WSe_2. (a) Optical microscope image of Sample #2 (356 nm top hBN/WSe_2 monolayer/56 nm bottom BN/FLG back gate/BK-7 glass substrate). A graphene finger is used to ground the WSe_2 flake and Cr/Au electrodes are made to both the graphene contact and back gate. Image labels are included in false-color overlays to enhance visibility of layers. (b) Integrated confocal PL map with laser spot fixed over the WSe_2 while the collection spot is scanned, showing waveguided PL collected when mapping over the hBN edges. Gate-dependent PL is taken in both (c) direct and (d) edge-collected configurations. Line cuts of gate-dependent PL are taken at the charge neutrality point (V_G = 0.25 V, indicated by dashed line in (c) and (d)) for both configurations in (e) and (f), respectively.

well as when the collection spot is scanned over the etched hBN edge away from the excitation spot (i.e., waveguided PL).

As exciton population in WSe_2 is highly dependent on the charge state, it is useful to tune the Fermi energy with electronic gating to discriminate between different states. Emerging topics in the 2D material field, such as highly correlated states, also rely heavily on electrical gating, therefore demonstrating the compatibility of our method with gating is of great interest. Gate voltage-dependent PL is performed when the collection spot is co-located with the excitation beam (local PL, Fig. 3c) and when the collection spot is fixed on one of the hBN edges (waveguided PL, Fig. 3d). The local PL shows exemplary gated-WSe_2 characteristics, with clear examples of the neutral exciton, biexciton (XX), negative (X^-) and positive (X^+) trions, the negative biexciton (XX^-), and additional exciton-phonon replica series which are beyond the scope of our study,[64] further indicating the high sample quality that can be achieved with hBN slab waveguides. The dark exciton (X_D) and trions ($X_D^{+/-}$) are also visible, but faint compared to the bright excitons. However, when using waveguide-based PL collection (spot B Fig. 3b), the dark exciton and trion signal are significantly enhanced relative to the bright exciton series. We show spectral line cuts near the charge neutrality point from the gate-dependent local (Fig. 3e) and waveguided PL (Fig. 3f). In the waveguiding collection channel, the X_D signal is around 11× stronger than X_0, and the reduction in background bright exciton emission reveals the coexistence of the dark trion state even close to charge neutrality. These results demonstrate that the effective capture of the dark exciton PL can be achieved with hBN encapsulation and waveguiding, all without compromising the electronic quality of monolayer TMD.

Our experimental results on the prototypical 2D semiconductors $MoSe_2$ and WSe_2 demonstrate that hBN encapsulation forming slab waveguides provides an effective route to studying PL of both IP and OP dipole emitters. To give a sense for the broad application opportunities afforded by hBN slab WGs, we have performed additional pilot studies. While we have presented PL collected from etched hBN edges here, we note that it is also possible to achieve the same behavior with naturally cleaved hBN edges (SI Fig. S1). Thus, our results may be replicated without any complicated lithography or etching. Further, we have performed Raman spectroscopy waveguiding measurements on Sample #1, which is promising for future explorations of mechanical properties of layered materials using a waveguide-based excitation/collection channel (SI Fig. S2). Given the opportunity for interdisciplinary studies using hBN slab waveguides that bridge the optical, electrical, and mechanical domains, we will conclude our work with a series of computational results that will serve as a structural design guide for making use of our technique.

3. COMPUTATIONAL RESULTS AND DISCUSSION

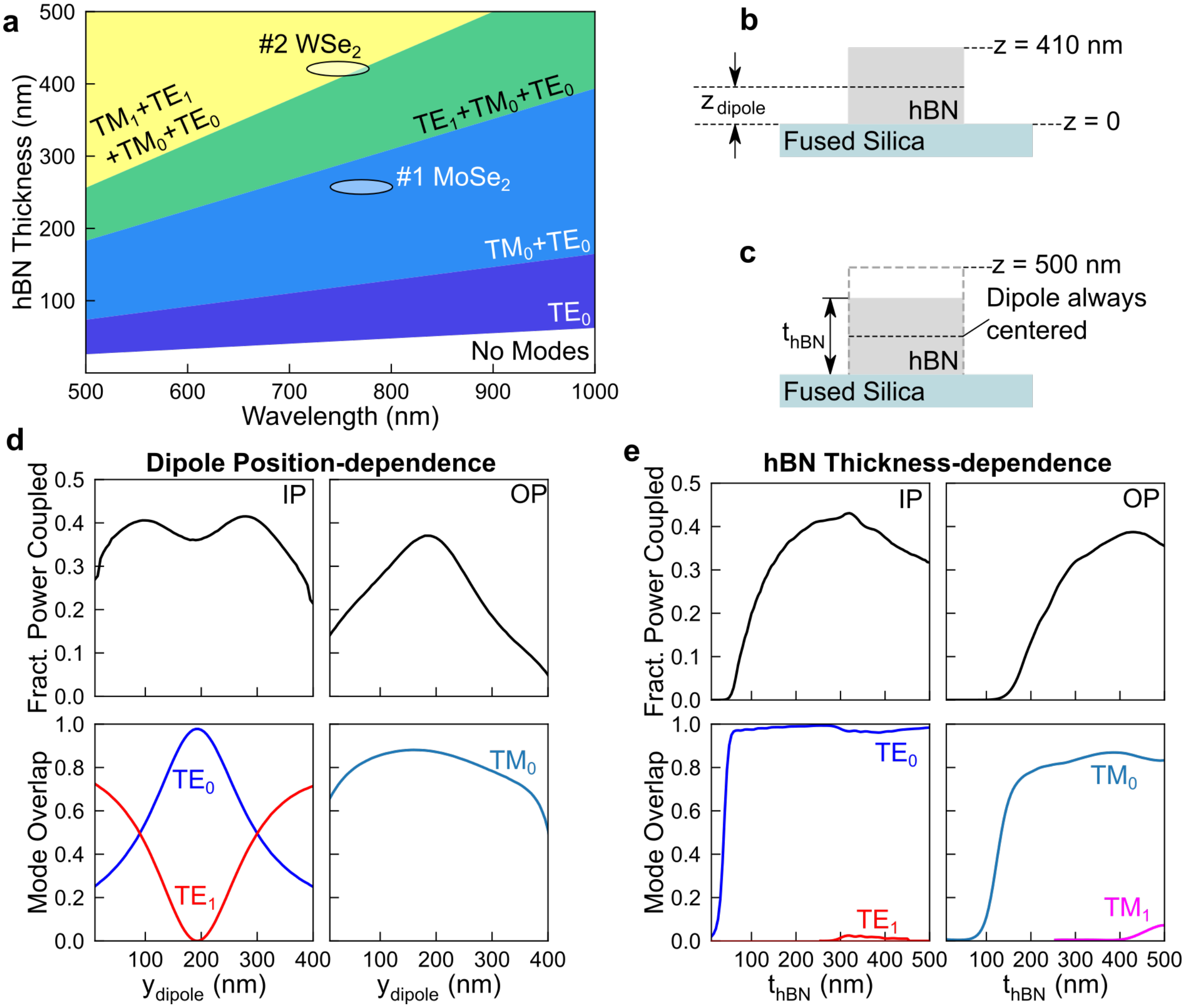

Figure 4: Slab waveguide coupling model (a) Allowed slab waveguide modes as a function of wavelength and hBN slab thickness, showing the first four modes (two TE, two TM). Ellipses are overlaid upon the plot to indicate the two samples examined in this work, with the range of exciton wavelengths expected for the corresponding TMDs. (b) Schematic of dipole placement study, where an IP or out-of-plane dipole is placed at various z-positions throughout a 410 nm hBN slab. (c) Schematic of hBN thickness study, where the hBN thickness is varied with an IP or OP dipole fixed in the center of the slab. (d) Dipole position-dependence calculations showing (top panels) fractional power coupled into the hBN slab for IP/OP dipoles and (bottom panels) corresponding mode overlap for occupied modes. (e) hBN thickness-dependent waveguiding with a dipole emitter fixed at half the thickness of the hBN slab, panels arranged as in (d).

To further enhance the utility of our results, and expand their applicability to future spectroscopy of layered materials, we now turn to computational modeling. We use our electromagnetic models to study important structural parameters for utilizing hBN slabs in optical experiments that will build intuition and provide guidelines which can be implemented in the field. We begin by calculating (see SI note S1.2) the number of occupied TE and TM modes in our slab waveguides (Fig. 4a) for a relevant range of thicknesses (up to 500 nm) and wavelengths (500 – 1000 nm). Our calculations indicate that single TE/TM mode operation is accessible for total slab thicknesses of 200 – 250 nm and spanning a wide range of relevant wavelengths for most 2D semiconductor optical properties. On the other hand, if waveguide coupling is considered disadvantageous, our results indicate that the total hBN thickness must remain under approximately 50 nm.

From a design standpoint, an important aspect of the van der Waals assembly process is our ability to arbitrarily position the dipole emitter (e.g., monolayer semiconductor) within the hBN slab waveguide (Fig 4b). Additionally, single-photon emitters (due to dopants or defects) in the hBN lattice can exist throughout the thickness of a given hBN slab. Therefore, we calculate the fractional power coupled into the hBN waveguide for IP and OP dipoles (Fig 4d, top panels) as a function of dipole placement along the *z*-axis. We consider a slab of 410 nm thick, matching the total hBN thickness of Sample #2. Our simulations are performed for $\lambda = 750$ nm, which is in-between the wavelengths of excitons studied throughout this paper, although we expect the trends observed to translate to similar wavelengths. Our simple WG mode population calculation indicates the slab can support up to four modes; however, our finite-element simulations indicate only the TE_0, TE_1, and TM_0 modes are well-guided while the TM_1 mode is lossy. Further, we calculate the overlap of the guided light with the eigenmodes of the infinite slab waveguide, indicating the position-dependent coupling to each transverse mode. The IP dipole configuration emits into TE_0 and TE_1 modes (Fig 4d, lower left) and the OP dipole emits into the TM_0 mode (Fig 4d, lower right). Our results indicate that most of the light emitted by the dipole in each case is guided in the first few modes, with less than 10% of the light guiding in leaky higher order modes or hybrid substrate modes.

The highest fractional power from the IP dipole coupled into the hBN WG occurs when the mode overlap is equally split between the TE_0 and TE_1 modes, at positions around 1/3 or 2/3 of the total hBN thicknesses. When the dipole is placed slightly below the center of the hBN, nearly all of the guided light is coupled into the TE_0 mode. Therefore, even for multi-TE-mode slabs, single-mode performance, which is less lossy and insensitive of path length from the emitter to hBN edge out-coupler, can be forced via stack geometry. For OP dipoles, which emit preferentially into TM modes, single-mode performance is guaranteed over a larger range than their IP dipole counterparts. However, we see that the guided fractional power of OP dipole emission is more sensitive to placement and should be placed towards the center of the hBN slab for optimal performance.

It is possible to encapsulate 2D layers with equal thickness top and bottom hBN layers by laterally dividing a single hBN flake by mechanical cracking or lithography. This approach is precise at the atomic layer level, which is unique to layered materials. Therefore, we calculated the thickness-dependent, guided power of light from emitters embedded in equal thickness top/bottom hBN slabs (schematically depicted in Fig. 4c). For the IP dipole (Fig 4e, top left), the peak in the guided fractional power occurs very close to the cut-on thickness of the TE_1 mode, just under 300 nm for this wavelength of light, however the majority (around 98%) of the light is guided in the TE_0 mode in this configuration (Fig 4e, bottom left). Similar behavior is shown for OP dipoles (Fig 4e, right panels), however the peak coupled power occurs in significantly thicker slabs (~400 nm), again marked by the cut-on thickness of the second TM mode.

Our computational models indicate that up to four guided modes (two TE, two TM) can be supported in typical hBN slab thicknesses used in 2D heterostructures. Dipole position within a given slab can be used to steer light into desired guided modes and nearly pure single-mode performance can be achieved regardless of the total slab thickness, simply by placing the emitter close to the center of the thickness of the stack. Close to optimal guiding performance for typical emission from TMDs can be achieved in the center-placement configuration by utilizing total thicknesses around 300 to 400 nm. These results provide a simple framework in which to operate for enhancing spectroscopic measurements of 2D materials with hBN waveguides. Furthermore, our results on guided mode-coupling effects will be useful for future optical devices integrating hBN and dipole emitters.

4. CONCLUSION

In conclusion, we have performed a combined experimental and computational study of hBN slab waveguides integrated with monolayer 2D semiconductors. We have shown how emission from both bright and dark excitons (i.e., in-plane and out-of-plane dipoles) can be guided effectively on standard substrates by selecting an appropriate hBN thicknesses. Fourier imaging indicates that a simple etched hBN edge is sufficient to direct guided light into the acceptance cone of standard objective lenses. We successfully integrated electrical gates into our waveguide to enable charge tuning of embedded layered materials during optical guiding experiments. We performed a comprehensive computational study to establish a design framework for maximizing coupling into and out of hBN slab waveguides. We find it is straightforward to couple emitted light directly to guided modes whilst maintaining a pristine dielectric environment around the emitter. These slab waveguides are highly versatile, performing well even using natural hBN edges. Additionally, Raman scattered light may be studied via waveguiding, which is promising for future studies on the optomechanical properties of 2D materials[65]. Our results enable rapid screening of existing layered material samples in the literature for the possibility of enhanced measurement by waveguiding. These results should enable future optical studies on 2D materials, particularly for multi-layer structures that support out-of-plane dipole emitters that are difficult to capture in conventional setups. Additionally, enhanced understanding of hBN slab waveguides paves the way for performing nonlinear optics in 2D materials, such as optical parametric amplification experiments,[66] with enhanced laser-interaction path lengths as well as simultaneous optical interrogation of networks of quantum dots in moiré-based heterostructures.[67]

5. EXPERIMENTAL SECTION

Sample fabrication: Samples are fabricated by mechanical exfoliation of hBN, $MoSe_2$, WSe_2, and graphite onto 90 nm dry thermal oxide on silicon. The $MoSe_2$ and WSe_2 crystals are flux-grown single crystals purchased from 2D semiconductors. Graphite is sourced as graphenium flakes from *NGS* Naturagraphit. Desired flake thicknesses are identified with optical contrast. Heterostructures are assembled via the van der Waals assembly method to ensure polymer-free interfaces. Microlens PDMS stamps are integrated with either polycarbonate (PC) or polyvinyl chloride (PVC) films and assembly is performed at temperatures exceeding 100 °C. Finished heterostructures are either released onto final substrates at 165 °C by melting the PC film, or direct release from PVC. PVC is used for ease of picking up few-layer graphite gates, such as the one in Sample #2. Finished structures are cleaned in dichloromethane and isopropyl alcohol (IPA). Atomic force microscopy (AFM) is performed with a Bruker Dimension FastSCAN AFM to determine the thickness of the 2D flakes. Electron beam lithography is performed in a Raith Voyager at 50 kV to pattern samples into desired shapes. ZEP 520A resist is spin-coated at 3000 RPM and baked at 150 °C for 2 minutes and then the negative tone of the desired pattern is exposed with an electron beam current around 0.2 nA to a dose of 200 $\mu C/cm^2$ with a step size of 4 nm. Room temperature development for 1 minute in ZED-N50 followed by IPA rinsing clears the exposed resist around the desired features, leaving a crisp etch mask. Dry etching of the hBN slab is performed in an Oxford Instruments PlasmaPro 80 RIE in a mixture of 100 sccm SF_6 and 10 sccm O_2 at 30 mTorr with 100 W forward RF power. The etch rate of hBN in this configuration is around 1 μm/minute and it produces sidewalls which are capable of coupling guided light to the farfield within the acceptance cone of standard air objectives. After RIE, the resist mask is removed by room temperature Remover PG followed by rinsing in acetone and IPA.

Optical Measurements: Three optical microscope setups are used in this work. The low temperature measurements are performed in a confocal microscope built around a Montana Cryostation with an integrated 0.75 NA objective and base sample temperature of 4.5 K. The system is equipped with two sets of galvanometer mirrors (Newport FSM-1) which are each coupled to single-mode fibers. One mirror steers a 532 nm diode laser (Coherent Sapphire) on the sample while the other images the mode profile of the PL collection fiber and sends collected light to a spectrometer equipped with a CCD (Princeton Instruments SCT-320 and Pylon). The image of each fiber on the sample produces two diffraction limited spots (one excitation, one collection) which can be steered independently. Prior to collection, the excitation laser is filtered from the PL using long-pass filters. Fourier microscopy is performed in a second setup in which the back focal plane of the microscope objective (0.8 NA) is imaged onto a CCD. The sample is excited with 514 nm laser light coupled from a multi-mode fiber which produces a large spot on the sample, close to the size of the TMD flake of interest. The multi-mode fiber scrambles the laser polarization, resulting in a weakly polarized excitation beam. The system is equipped with a pinhole placed in a real-space image plane which facilitates Fourier imaging of PL from specific spatial locations on the sample. Raman measurements of Sample #1 and PL mapping of Sample #3 are performed in a third optical microscope which is equipped with a 488 nm laser and volume holographic Bragg filters which filter the excitation laser.

6. SUPPORTING INFORMATION

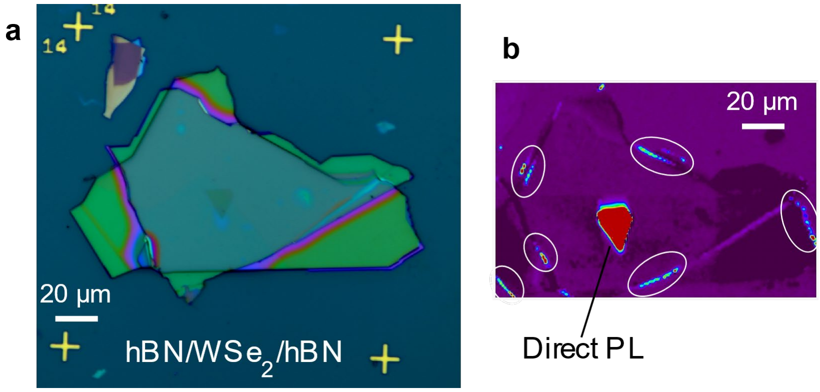

Figure S1: Waveguiding of WSe$_2$ PL in an un-patterned hBN slab waveguide. (a) As-assembled heterostructure consisting of hBN/monolayer WSe$_2$/hBN laminated to a 270 nm SiO$_2$/Si substrate. (b) Laser scanning photoluminescence map of WSe$_2$ PL. Typical direct PL is observed as the laser scans over the triangular WSe$_2$ monolayer. Spots along the natural hBN edges, many examples of waveguide-coupled PL is observed (circled in white). In this measurement configuration, the laser first couples into the waveguide and excites the WSe$_2$, and then the corresponding PL is coupled back into the waveguide and out to the far-field at the same spot on the edge. This result highlights that our technique may be applied without the use of any lithography, just using standard 2D material stacking techniques.

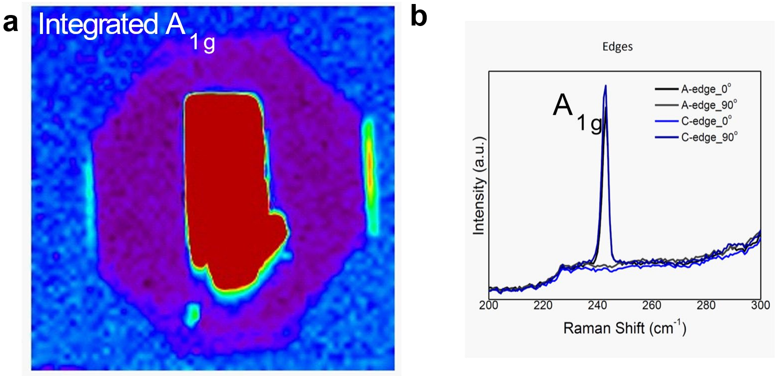

Figure S2: Waveguiding of Raman scattered light from $MoSe_2$. (a) Map of integrated Raman intensity for the $MoSe_2$ A_{1g} mode. The Raman signal is filtered with a vertical linear polarizer, thus edge-coupled intensity is only seen for the edges of the octagonal hBN slab oriented vertically. (b) Raman spectra collected by exciting/collecting from the hBN slab edges. In order to verify that the WG signal only seen on the vertical edges is due to polarization and not a peculiarity of the sample, we measure signals from two orthogonal edges and then rotate the sample and measure the same edges again. In each case, only the edge which is vertical (parallel with the linear polarization detection of our microscope) shows a Raman signal.

Section S1: Computational methods

7. S1.1 SIMULATED FOURIER (K-SPACE) IMAGES

From Fraunhofer diffraction theory, the scalar electric field in the far field due to a near-field diffracting object, such as an aperture, is equal to:

$$\hat{E}(x',y',L) = \mathcal{F}\big(E(x,y,0)\big) \quad (2)$$

where $\hat{E}$ is the scalar far field at position L from the diffracting object with spatial coordinates of x' and y', E is the electric field in the near field at the plane of the diffracting object ($z = 0$) with spatial coordinates of x and y. $\mathcal{F}(\cdot)$ denotes the 2D spatial Fourier transform. In the current work, we simulate the electromagnetic wave propagation within a 3D geometry, then define an artificial surface within the geometry as use that as our near field aperture. The 3D geometry consists of a substrate with dimensions 8λ by 8λ and 270 nm thick and a layer of air on top with the same area and height of 4λ. Embedded within the air layer and resting on the substrate, we place a slab of hBN that is 8λ wide and 4λ long, where the edge of the hBN slab is centered in the simulation domain. This entire structure is then bordered by PMLs except for the bottom of the 270 nm substrate, where we instead include an impedance boundary condition using the material properties of Si. Without the impedance boundary condition the air/hBN/SiO_2 system is lossless. With the inclusion of the impedance boundary condition the effective index of the TE_0 and TM_0 modes become complex stemming from loss in the Si substrate.

To focus specifically on the guided modes with the hBN waveguides, we define a numeric port with a width of λ centered laterally along the hBN slab at the PML/hBN interface (see Fig. S3a). This port extends from the bottom of the substrate (at -270 nm from the hBN surface) to the top of the air domain, not including the PML at the top. We perform a boundary mode analysis to determine the effective index of the TE_0 and TM_0 modes, then assign those modes in two separate simulations, one for the TE_0 (n_{eff}=1.82695-i4.4674x10^{-4}) and one for the TM_0 (n_{eff}=1.58034-i1.0706x10^{-2}). Following the simulation, we employ COMSOL's spatial FFT solver using the field at the artificial layer 0.3 μm from the top of the hBN slab to act as the aperture. The PML regions surrounding the slab are not included, instead, we use zero padding in both the x and y dimensions. The spatial FFT settings are provided in Fig. S3(b).

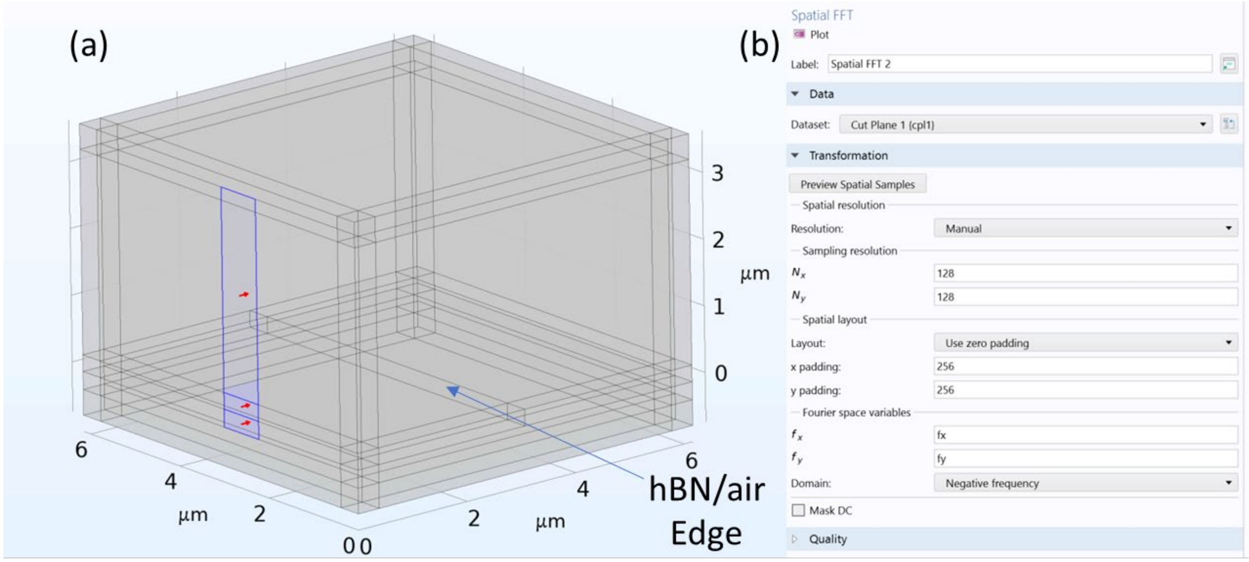

Spatial FFT
Plot
Label: Spatial FFT 2
Data
Dataset: Cut Plane 1 (cpl1)
Transformation
Preview Spatial Samples
Spatial resolution
Resolution: Manual
Sampling resolution
N_x 128
N_y 128
Spatial layout
Layout: Use zero padding
x padding: 256
y padding: 256
Fourier space variables
f_x fx
f_y fy
Domain: Negative frequency
☐ Mask DC
Quality

Figure S3: Configuration of 3D electromagnetic waveguide model. (a) 3D COMSOL geometry for simulated Fourier imaging from hBN edges. The highlighted region shows the location of the numeric port for injecting guided modes, and the hBN is also highlighted. (b) Settings in the COMSOL used for the spatial FFT solver.

As a verification of the FFT analysis methodology, we offset the location of the numerical port to λ/2 away from the edge of the PLM in the -y-direction (Fig. S4(a)). This effectively eliminates all of the emission along the -y-direction since it is strongly absorbed by the PML. We clearly observe this behavior in the simulated Fourier images of Fig. S4(b,c) where the FFT of the separate field components, E_y and E_x, show the absence of, or significant reduction in intensity in the -k$_y$ region of the simulated images, respectfully. These simulations correspond with the polarizer along the edge or perpendicular to the edge, respectfully.

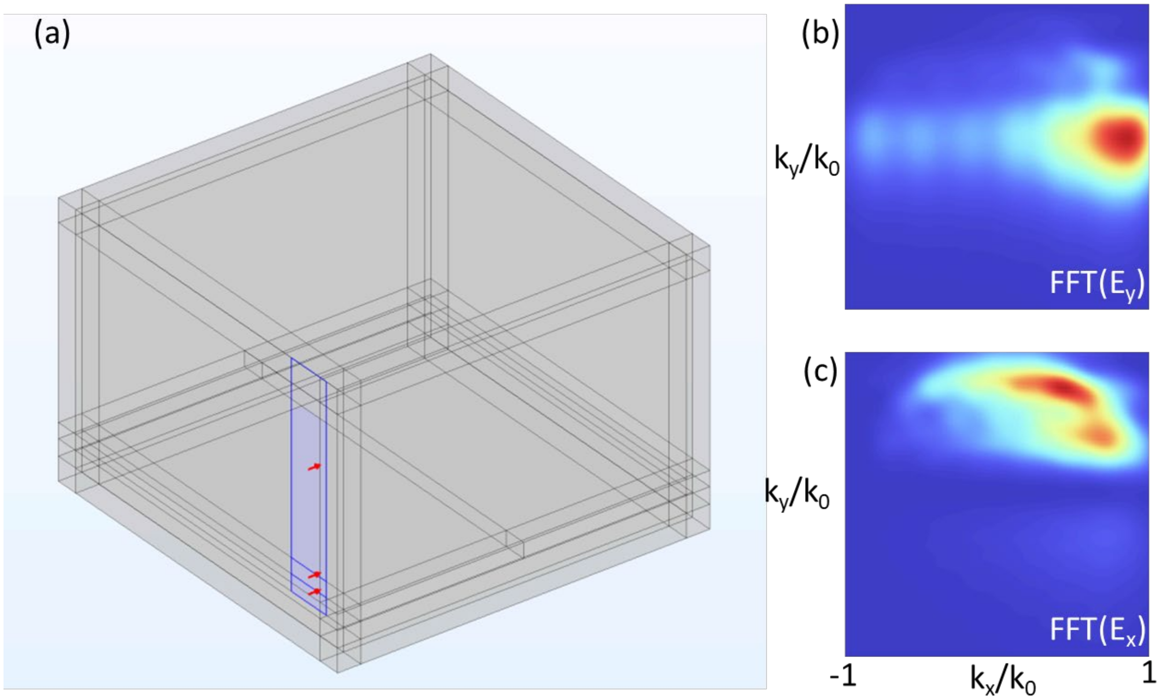

Figure S4: Waveguiding simulation with restricted angles. (a) 3D COMSOL geometry with edge of port aligned λ/2 from the edge of the simulation domain (along the -y-direction). (b) Simulated Fourier image based on the FFT of the nearfield E_y intensity, and (c) simulated Fourier image based on the FFT of the nearfield E_x intensity. The corresponding orientations of a polarizer in the experiment would be along the edge and perpendicular to the edge of the hBN slab in parts (b) and (c), respectively.

S1.2 Effective index of refraction for propagating TE and TM modes in hBN

We computed the effective index of refraction for propagating TE and TM modes in hBN by solving the transcendental equations[1]:

$$k_0 d\sqrt{n_o^2 - n_{\text{eff,TE}}^2} = \tan^{-1}\left(\frac{\sqrt{n_{\text{eff,TE}}^2 - n_1^2}}{\sqrt{n_o^2 - n_{\text{eff,TE}}^2}}\right) + \tan^{-1}\left(\frac{\sqrt{n_{\text{eff,TE}}^2 - n_2^2}}{\sqrt{n_o^2 - n_{\text{eff,TE}}^2}}\right) + p\pi \qquad (1)$$

$$k_0 \frac{n_o}{n_e} d\sqrt{n_e^2 - n_{\text{eff,TM}}^2} = \tan^{-1}\left(\frac{n_o n_e}{n_1^2}\frac{\sqrt{n_{\text{eff,TM}}^2 - n_1^2}}{\sqrt{n_e^2 - n_{\text{eff,TM}}^2}}\right) + \tan^{-1}\left(\frac{n_o n_e}{n_2^2}\frac{\sqrt{n_{\text{eff,TM}}^2 - n_2^2}}{\sqrt{n_e^2 - n_{\text{eff,TM}}^2}}\right) + p\pi \qquad (2)$$

where k_0 is the free space wavevector, d the film thickness, p is the mode number starting at zero, and n_o, n_e, n_1, and n_2 are the ordinary and extraordinary index of refraction of hBN, the superstrate (air = 1), and substrate (SiO_2 =1.46), respectively. To solve, all terms are moved to one side of the equation and minimized with the use of MATLAB's fminsearch function by adjusting the value of $n_{\text{eff,TE}}$ and $n_{\text{eff,TM}}$ in equation (1) and equation (2), respectively. Both effective indices were calculated for wavelengths ranging from 250 nm to 1250 nm and thicknesses ranging from 10 nm to 500 nm. The wavelength dependent index of refraction were from Rah et al.[2] Contour maps for the different modes are provided in Fig. S5a-d and a phase map of the guided modes is displayed in Fig. S5e.

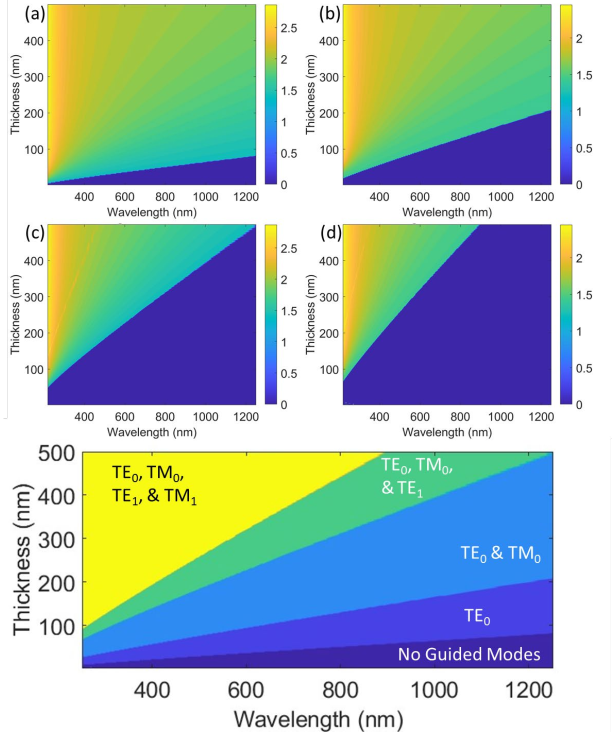

Figure S5: Calculations of hBN slab WG mode population. Contour plots of the effective index for (a) TE_0, (b) TM_0, (c) TE_1, and (d) TM_1 along with (e) the full phase map showing the thicknesses and wavelengths where the different modes are active in the films.

8. S1.1 POWER AND MODAL COUPLING ANALYSIS:

Fig. S6 provides an overview of the dipole coupling analysis. In COMSOL Multiphysics we define a 2D geometry for this analysis, where the substrate was either 270 nm of SiO_2 on Si (with a thickness of $\lambda/2$) or 270 nm of fused silica on an additional fused silica substrate (with thickness of $\lambda/2$). We placed the hBN layer above the substrate with thicknesses that ranged from 10 – 500 nm depending on the simulation. At the midpoint of the hBN region laterally, we define a point in the geometry which serves as the location for the dipole emitter. The layer of air above had a thickness of 6 λ, and outside all 4 boundaries we included perfectly matched layers (PMLs) with a thickness of $\lambda/4$ (orange region in Fig. S6a). For materials properties, especially the index of refraction, we used the built-in parameters provided by COMSOL's optical materials database for air, Si (Schinke et al., 2015), SiO_2 (Gao et al., 2013), and Schott N-BK10 glass, and created a user defined material for hBN based on Y. Rah, et al.[2] that includes both the in-plane and out-of-plane index of refraction.

To quantify the fraction power guided within the hBN slab, we integrate the outgoing power flow (COMSOL variable ewfd.nPoav) along the top and bottom boundaries of the hBN slab and along two artificial boundaries placed a distance of λ from the inside of the PML layers (black box in Fig. S6). The artificial boundaries have no impact on the model physics, but are offset from the PML to ensure no unwanted edge effects or reflections are included in the analysis. The guided fraction is then calculated by dividing the power flow from one edge (e.g., dashed black line in Fig. S6a) by the total power outflow integrated over all four edges (Fig. S6b).

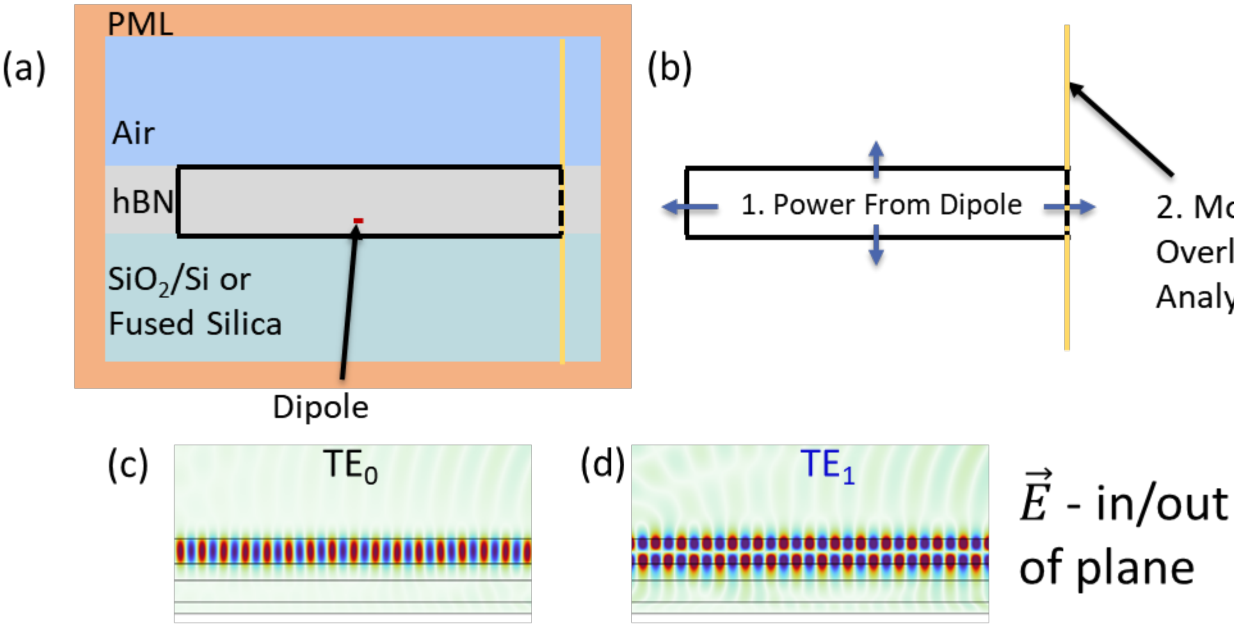

Figure S6: Dipole coupling analysis schematics. Geometry of the 2D simulations performed to quantify power coupling and mode overlap analysis, where (a) depicts the layers and material (b) shows how the power emits from the dipole and the location of the mode overlap analysis. (c,d) Surface maps depicting the in/out-of-plane E_z field profile for a guided TE_0 and a TE_1 mode, respectively. The TM_0 mode looks nearly identical to the TE_0 mode but it is oriented along the plane (E_y).

In addition to evaluating the total power emitted by the dipole, we also define listener ports at the artificial boundaries which span the substrate, hBN, and air domains as depicted by the yellow line in Fig. S6a-b). This is necessary to capture the full modal extent since a non-negligible fraction of the mode volume extends into the air and substrate. At the artificial boundary, we define four ports, each with a different effective index (computed) and corresponding with the TE_0, TM_0, TE_1, and TM_1 mode, respectively. To begin each simulation, four boundary mode analysis steps are performed to obtain the electric profiles corresponding to the pure guided modes. Examples of the TE_0, TE_1, and TM_0, are provided in Fig. S7 for a 405 nm hBN slab on glass.

Following the boundary mode analysis steps, COMSOL solves the full-field wave equation in the frequency domain wherein either a vertical magnetic dipole or a vertical electric dipole is used as the power source. The vertical magnetic dipole results in a transverse electric field (transvers to the simulation plane) yielding primarily TE oriented waves that propagate along the $\pm x$ direction approximating the response of in-plane (IP) exciton emission from TMDs.

At the artificial boundary, we extract the computed electric field profile of the waveguide, E_{wg} due to the dipole excitation. In Fig. S7a-b we display the electric field profiles E_{wg} for vertical magnetic dipoles centered vertically in the hBN slab Fig. S7a and offset to 55 nm above the substrate Fig. S7b. as gray dashed lines. When centered in the hBN, the field profile has very good overlap with the TE_0 guided mode. In contrast, the dipole offset to the bottom of the slab shows a partial overlap with both the TE_0 and the TE_1 modes. In Fig. S7c and S5d a vertical electric dipole is simulated yielding an in-plane electric field and therefore a transverse magnetic guided mode. We observe significant overlap between this waveguide mode (E_{wg}) (gray dashed lines) and the TM_0 guided mode (red lines) for both the centered dipole and offset dipole locations. We note that in Fig. S7a-b the normalized electric field into the plane (E_z) is depicted while in Fig. S7c-d the normalized electric field in the vertical direction (E_y) is depicted. In these 2D simulations the propagation direction is assumed to be strictly in the plane and thus only the pure TE and TM modes are computed. Moreover, due to the definition of the dipoles, the field is strictly confined to either the in-plane or out of plane directions, no cross over occurs.

For a more rigorous analysis of modal content, we compute the mode overlap based on equation (1):

$$\text{Mode Overlap} = \frac{\left|\iint \vec{E}_{mode}\vec{E}_{wg}^{*}dydz\right|^{2}}{\iint\left|\vec{E}_{wg}\right|^{2}dydz\cdot\iint\left|\vec{E}_{mode}\right|^{2}dydz} \quad (1)$$

where $\vec{E}_{mode}$ are the pure guided mode electric field profiles (TE_0, TE_1, TM_0, TM_1), and $\vec{E}_{wg}$ is the computed field due to guided light from the dipole. For our 2D simulations, the field into-the plane is constant so the integration occurs along the y-direct of the boundary. In 3D simulations, the cross-sectional integration would be used.

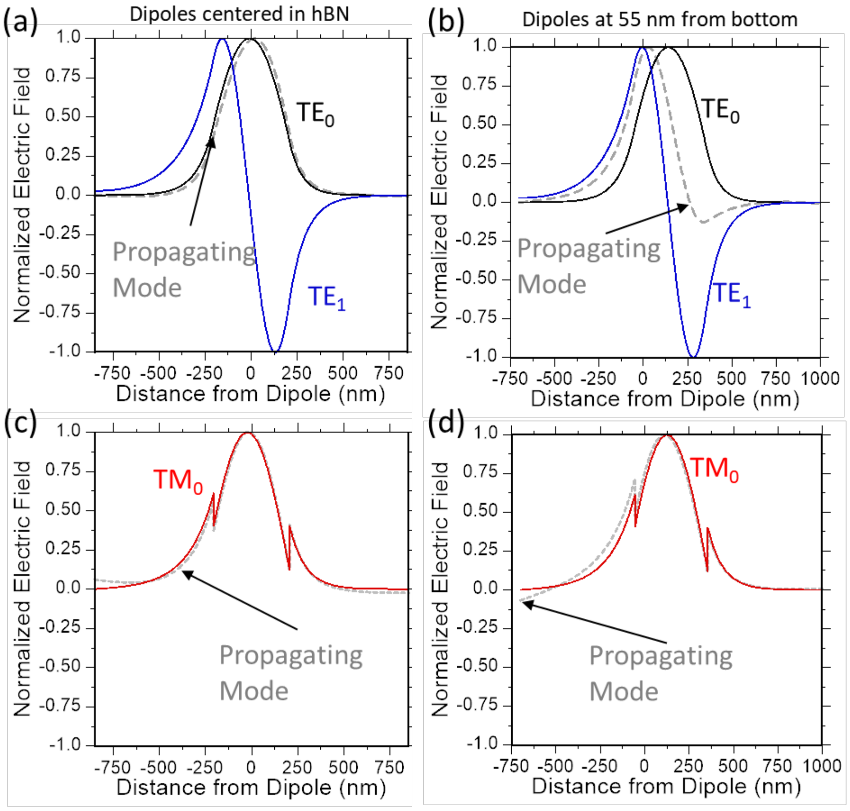

Figure S7: Coupling of dipole emitters to guided modes. Normalized electric field for (a,b) for the TE_0 (black lines) and TE_1 (blue lines) and (c,d) for the TM_0 (red lines) computed based on a boundary mode analysis for a 405 nm hBN slab on glass at λ=750 nm. In (a,c) the dipole emitter is centered vertically within the hBN slab, while in (b,d) the dipole is offset to 55 nm above the substrate (within the hBN) consistent with our WSe_2 samples. In (a,b) a vertical (out-of-plane) magnetic dipole is used to simulate an electric dipole that is oriented into the plane of the hBN slab (*i.e.,* orthogonal to the plane of the 2D simulation). In (c,d) a vertical (out-of-plane) electric dipole is used to simulate the out-of-plane the emission dipole of the dark exciton in WSe_2.

Acknowledgments

SWL acknowledges support for this work by the Jerome and Isabella Karles Distinguished Scholar Fellowship.

REFERENCES

1. Geim, A. K. & Grigorieva, I. V. Van der Waals heterostructures. *Nature* **499**, 419–425 (2013).
2. Ma, Q., Ren, G., Xu, K. & Ou, J. Z. Tunable Optical Properties of 2D Materials and Their Applications. *Adv. Opt. Mater.* **9**, 2001313 (2021).
3. Wang, Q. H., Kalantar-Zadeh, K., Kis, A., Coleman, J. N. & Strano, M. S. Electronics and optoelectronics of two-dimensional transition metal dichalcogenides. *Nat. Nanotechnol.* **7**, 699–712 (2012).
4. Xia, F., Wang, H., Xiao, D., Dubey, M. & Ramasubramaniam, A. Two-dimensional material nanophotonics. *Nat. Photonics* **8**, 899–907 (2014).
5. Mak, K. F. & Shan, J. Photonics and optoelectronics of 2D semiconductor transition metal dichalcogenides. *Nat. Photonics* **10**, 216–226 (2016).
6. Liu, X. & Hersam, M. C. 2D materials for quantum information science. *Nat. Rev. Mater.* **4**, 669–684 (2019).
7. Ma, N. & Jena, D. Charge Scattering and Mobility in Atomically Thin Semiconductors. *Phys. Rev. X* **4**, 011043 (2014).
8. Chen, J.-H. *et al.* Charged-impurity scattering in graphene. *Nat. Phys.* **4**, 377–381 (2008).
9. Rhodes, D., Chae, S. H., Ribeiro-Palau, R. & Hone, J. Disorder in van der Waals heterostructures of 2D materials. *Nat. Mater.* **18**, 541–549 (2019).
10. Shin, B. G. *et al.* Indirect Bandgap Puddles in Monolayer MoS2 by Substrate-Induced Local Strain. *Adv. Mater.* **28**, 9378–9384 (2016).
11. Zhang, Y., Brar, V. W., Girit, C., Zettl, A. & Crommie, M. F. Origin of spatial charge inhomogeneity in graphene. *Nat. Phys.* **5**, 722–726 (2009).
12. Gao, J. *et al.* Aging of Transition Metal Dichalcogenide Monolayers. *ACS Nano* **10**, 2628–2635 (2016).
13. Wood, J. D. *et al.* Effective Passivation of Exfoliated Black Phosphorus Transistors against Ambient Degradation. *Nano Lett.* **14**, 6964–6970 (2014).
14. Favron, A. *et al.* Photooxidation and quantum confinement effects in exfoliated black phosphorus. *Nat. Mater.* **14**, 826–832 (2015).
15. Decker, R. *et al.* Local Electronic Properties of Graphene on a BN Substrate via Scanning Tunneling Microscopy. *Nano Lett.* **11**, 2291–2295 (2011).
16. Dean, C. R. *et al.* Boron nitride substrates for high-quality graphene electronics. *Nat. Nanotechnol.* **5**, 722–726 (2010).
17. Xue, J. *et al.* Scanning tunnelling microscopy and spectroscopy of ultra-flat graphene on hexagonal boron nitride. *Nat. Mater.* **10**, 282–285 (2011).
18. Lee, G.-H. *et al.* Highly Stable, Dual-Gated MoS2 Transistors Encapsulated by Hexagonal Boron Nitride with Gate-Controllable Contact, Resistance, and Threshold Voltage. *ACS Nano* **9**, 7019–7026 (2015).
19. Wang, L. *et al.* Negligible Environmental Sensitivity of Graphene in a Hexagonal Boron Nitride/Graphene/h-BN Sandwich Structure. *ACS Nano* **6**, 9314–9319 (2012).

20. Huang, B. *et al.* Layer-dependent ferromagnetism in a van der Waals crystal down to the monolayer limit. *Nature* **546**, 270–273 (2017).
21. Scuri, G. *et al.* Large Excitonic Reflectivity of Monolayer ${\mathrm{MoSe}}_{2}$ Encapsulated in Hexagonal Boron Nitride. *Phys. Rev. Lett.* **120**, 037402 (2018).
22. Mayorov, A. S. *et al.* Micrometer-Scale Ballistic Transport in Encapsulated Graphene at Room Temperature. *Nano Lett.* **11**, 2396–2399 (2011).
23. Dean, C. R. *et al.* Multicomponent fractional quantum Hall effect in graphene. *Nat. Phys.* **7**, 693–696 (2011).
24. Wang, L. *et al.* One-Dimensional Electrical Contact to a Two-Dimensional Material. *Science* **342**, 614–617 (2013).
25. LaGasse, S. W., Dhakras, P., Watanabe, K., Taniguchi, T. & Lee, J. U. Gate-Tunable Graphene–WSe_2 Heterojunctions at the Schottky–Mott Limit. *Adv. Mater.* **31**, 1901392 (2019).
26. Kim, K. *et al.* van der Waals Heterostructures with High Accuracy Rotational Alignment. *Nano Lett.* **16**, 1989–1995 (2016).
27. Cao, Y. *et al.* Unconventional superconductivity in magic-angle graphene superlattices. *Nature* **556**, 43–50 (2018).
28. Cao, Y. *et al.* Correlated insulator behaviour at half-filling in magic-angle graphene superlattices. *Nature* **556**, 80–84 (2018).
29. Li, H. *et al.* Imaging local discharge cascades for correlated electrons in WS2/WSe2 moiré superlattices. *Nat. Phys.* **17**, 1114–1119 (2021).
30. Zhou, Y. *et al.* Bilayer Wigner crystals in a transition metal dichalcogenide heterostructure. *Nature* **595**, 48–52 (2021).
31. Regan, E. C. *et al.* Mott and generalized Wigner crystal states in WSe2/WS2 moiré superlattices. *Nature* **579**, 359–363 (2020).
32. Smoleński, T. *et al.* Signatures of Wigner crystal of electrons in a monolayer semiconductor. *Nature* **595**, 53–57 (2021).
33. Xu, Y. *et al.* A tunable bilayer Hubbard model in twisted WSe2. *Nat. Nanotechnol.* **17**, 934–939 (2022).
34. Tang, Y. *et al.* Simulation of Hubbard model physics in WSe2/WS2 moiré superlattices. *Nature* **579**, 353–358 (2020).
35. Gu, J. *et al.* Dipolar excitonic insulator in a moiré lattice. *Nat. Phys.* **18**, 395–400 (2022).
36. Fang, N. *et al.* Hexagonal Boron Nitride As an Ideal Substrate for Carbon Nanotube Photonics. *ACS Photonics* **7**, 1773–1779 (2020).
37. Huang, J.-W. *et al.* Superior Current Carrying Capacity of Boron Nitride Encapsulated Carbon Nanotubes with Zero-Dimensional Contacts. *Nano Lett.* **15**, 6836–6840 (2015).
38. Seitz, M., Gant, P., Castellanos-Gomez, A. & Prins, F. Long-Term Stabilization of Two-Dimensional Perovskites by Encapsulation with Hexagonal Boron Nitride. *Nanomaterials* **9**, 1120 (2019).
39. Fang, H.-H. *et al.* Unravelling Light-Induced Degradation of Layered Perovskite Crystals and Design of Efficient Encapsulation for Improved Photostability. *Adv. Funct. Mater.* **28**, 1800305 (2018).
40. Yu, H. *et al.* Waterproof Perovskite-Hexagonal Boron Nitride Hybrid Nanolasers with Low Lasing Thresholds and High Operating Temperature. *ACS Photonics* **5**, 4520–4528 (2018).
41. Scavuzzo, A. *et al.* Electrically tunable quantum emitters in an ultrathin graphene–hexagonal boron nitride van der Waals heterostructure. *Appl. Phys. Lett.* **114**, 062104 (2019).
42. Dietrich, A., Doherty, M. W., Aharonovich, I. & Kubanek, A. Solid-state single photon source with Fourier transform limited lines at room temperature. *Phys. Rev. B* **101**, 081401 (2020).
43. Grosso, G. *et al.* Tunable and high-purity room temperature single-photon emission from atomic defects in hexagonal boron nitride. *Nat. Commun.* **8**, 705 (2017).

44. Proscia, N. V. *et al.* Near-deterministic activation of room-temperature quantum emitters in hexagonal boron nitride. *Optica* **5**, 1128–1134 (2018).
45. Gottscholl, A. *et al.* Initialization and read-out of intrinsic spin defects in a van der Waals crystal at room temperature. *Nat. Mater.* **19**, 540–545 (2020).
46. Dai, S. *et al.* Subdiffractional focusing and guiding of polaritonic rays in a natural hyperbolic material. *Nat. Commun.* **6**, 6963 (2015).
47. He, M. *et al.* Guided Mid-IR and Near-IR Light within a Hybrid Hyperbolic-Material/Silicon Waveguide Heterostructure. *Adv. Mater.* **33**, 2004305 (2021).
48. Mak, K. F., Lee, C., Hone, J., Shan, J. & Heinz, T. F. Atomically Thin ${\mathrm{MoS}}_{2}$: A New Direct-Gap Semiconductor. *Phys. Rev. Lett.* **105**, 136805 (2010).
49. Cheiwchanchamnangij, T. & Lambrecht, W. R. L. Quasiparticle band structure calculation of monolayer, bilayer, and bulk MoS${}_{2}$. *Phys. Rev. B* **85**, 205302 (2012).
50. Ramasubramaniam, A. Large excitonic effects in monolayers of molybdenum and tungsten dichalcogenides. *Phys. Rev. B* **86**, 115409 (2012).
51. Qiu, D. Y., da Jornada, F. H. & Louie, S. G. Optical Spectrum of ${\mathrm{MoS}}_{2}$: Many-Body Effects and Diversity of Exciton States. *Phys. Rev. Lett.* **111**, 216805 (2013).
52. Chernikov, A. *et al.* Exciton Binding Energy and Nonhydrogenic Rydberg Series in Monolayer ${\mathrm{WS}}_{2}$. *Phys. Rev. Lett.* **113**, 076802 (2014).
53. Wang, G. *et al.* Colloquium: Excitons in atomically thin transition metal dichalcogenides. *Rev. Mod. Phys.* **90**, 021001 (2018).
54. Park, K.-D., Jiang, T., Clark, G., Xu, X. & Raschke, M. B. Radiative control of dark excitons at room temperature by nano-optical antenna-tip Purcell effect. *Nat. Nanotechnol.* **13**, 59–64 (2018).
55. Lo, T. W. *et al.* Plasmonic Nanocavity Induced Coupling and Boost of Dark Excitons in Monolayer WSe2 at Room Temperature. *Nano Lett.* **22**, 1915–1921 (2022).
56. Zhou, Y. *et al.* Probing dark excitons in atomically thin semiconductors via near-field coupling to surface plasmon polaritons. *Nat. Nanotechnol.* **12**, 856–860 (2017).
57. Gelly, R. J. *et al.* Probing dark exciton navigation through a local strain landscape in a WSe2 monolayer. *Nat. Commun.* **13**, 232 (2022).
58. Tang, Y., Mak, K. F. & Shan, J. Long valley lifetime of dark excitons in single-layer WSe2. *Nat. Commun.* **10**, 4047 (2019).
59. Khelifa, R. *et al.* Coupling Interlayer Excitons to Whispering Gallery Modes in van der Waals Heterostructures. *Nano Lett.* **20**, 6155–6161 (2020).
60. Khelifa, R. *et al.* WSe2 Light-Emitting Device Coupled to an h-BN Waveguide. *ACS Photonics* (2023) doi:10.1021/acsphotonics.2c01963.
61. Aly, M. A. *et al.* Radiative pattern of intralayer and interlayer excitons in two-dimensional WS2/WSe2 heterostructure. *Sci. Rep.* **12**, 6939 (2022).
62. Brotons-Gisbert, M. *et al.* Out-of-plane orientation of luminescent excitons in two-dimensional indium selenide. *Nat. Commun.* **10**, 3913 (2019).
63. Jackson, John D. *Classical electrodynamics*. (Wiley, 1999).
64. He, M. *et al.* Valley phonons and exciton complexes in a monolayer semiconductor. *Nat. Commun.* **11**, 618 (2020).
65. Zalalutdinov, M. K. *et al.* Acoustic cavities in 2D heterostructures. *Nat. Commun.* **12**, 3267 (2021).
66. Trovatello, C. *et al.* Optical parametric amplification by monolayer transition metal dichalcogenides. *Nat. Photonics* **15**, 6–10 (2021).
67. Baek, H. *et al.* Highly energy-tunable quantum light from moiré-trapped excitons. *Sci. Adv.* **6**, eaba8526 (2020).